

Active Components for 50 Gb/s NRZ-OOK Optical Interconnects in a Silicon Photonics Platform

M. Pantouvaki, *Member, IEEE*, S. A. Srinivasan, Y. Ban, P. De Heyn, P. Verheyen, G. Lepage, H. Chen, J. De Coster, N. Golshani, S. Balakrishnan, P. Absil, and J. Van Campenhout, *Member, IEEE*

(Invited Paper)

Abstract—We present active components developed in imec’s silicon photonics platform that enable 50-Gb/s non-return-to-zero operation using CMOS compatible voltages.

Index Terms—Electrooptic modulators, integrated optoelectronics, optical interconnects, optical receivers, optical transmitters, photodetectors, photonic integrated circuits, silicon photonics.

I. INTRODUCTION

WITH growing bandwidth requirements for interconnects in datacenters and for I/O in high-performance processors, it is becoming increasingly important to improve the link power efficiency and bandwidth density for realizing continued system scaling. Optical interconnects are becoming attractive at progressively shorter link distances, as they can provide higher bandwidth density with potentially lower power consumption as compared to Cu interconnects [1], [2]. In order for optical interconnects to become economically viable, the operational and the production costs have to be reduced below that of Cu interconnects, while delivering higher performance.

Silicon photonics technology can potentially reduce the fabrication cost of integrated photonics components and systems, by re-using existing CMOS fabrication infrastructure while delivering high volumes at high yield. High-bandwidth optical transceivers have been recently demonstrated using silicon photonics components [3]–[7]. In [8], [9] we presented imec’s silicon photonics platform that co-integrates passive components with modulators and photodetectors operating up to 28 Gb/s. In this paper we present active components such as modulators and photodetectors that demonstrate non-return-to-zero (NRZ) on-off keying (OOK) modulation or detection at 50 Gb/s or higher, using CMOS-compatible voltages.

Manuscript received June 14, 2016; revised August 12, 2016; accepted August 17, 2016. Date of publication August 31, 2016; date of current version February 22, 2017.

The authors are with the Interuniversity Microelectronics Center, Heverlee 3001, Belgium (e-mail: pantouv@imec.be; ashwyn.srinivasan@imec.be; Yoojin.Ban@imec.be; Peter.DeHeyn@imec.be; peter.verheyen@imec.be; guy.lepage@imec.be; Hongtao.Chen@imec.be; Jeroen.DeCoster@imec.be; Negin.Golshani@imec.be; Sathishkumar.Balakrishnan@imec.be; absilp@imec.be; joris.vancampenhout@imec.be).

Color versions of one or more of the figures in this paper are available online at <http://ieeexplore.ieee.org>.

Digital Object Identifier 10.1109/JLT.2016.2604839

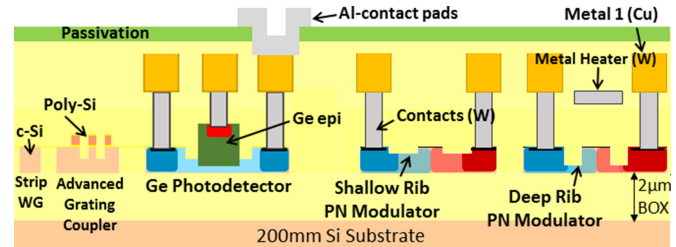


Fig. 1. Schematic cross-section of imec’s silicon photonics platform, indicating basic passive and active devices.

II. DEVICE FABRICATION

The devices presented in this paper were fabricated in a 200 mm or 300 mm silicon photonics platform using silicon-on-insulator (SOI) wafers with 220 nm top crystalline silicon and 2 µm buried oxide (BOX). A schematic cross-section of imec’s platform indicating some basic devices is shown in Fig. 1. Standard CMOS-compatible processing using 193 nm lithography for waveguide patterning and copper (Cu)-based back-end metallization were used for device and contact fabrication in both the 200 mm and 300 mm platforms. The 300 mm platform offers the additional advantage of 193 nm immersion lithography, which was not critical for achieving the device performance demonstrated in this paper, but can be used to further extend the platform to more advanced devices in future.

The top silicon layer of the SOI is used to form passive components such as waveguides, multiplexers / de-multiplexers, fiber-grating couplers, and silicon-based modulators. To enable a variety of components three silicon waveguide patterning steps are used, with etch depths of 220 nm, 150 nm and 70 nm. After patterning, the waveguides are planarized using an oxide cladding. Additional device functionality is enabled by depositing a 160 nm thick poly-silicon layer on top, which is patterned in one step. The silicon is doped using three implantation steps for p-type and three for n-type doping. After oxide planarization of the poly-silicon structures and implant activation anneal, windows are opened in the planarized oxide, and Ge or GeSi is selectively grown in these windows using reduced-pressure chemical vapor deposition (RP-CVD). Excessive Ge is removed by chemical-mechanical polishing and p-type or n-type doping is incorporated in the Ge areas by ion implantation and activation anneal. This module enables Ge-based electro-

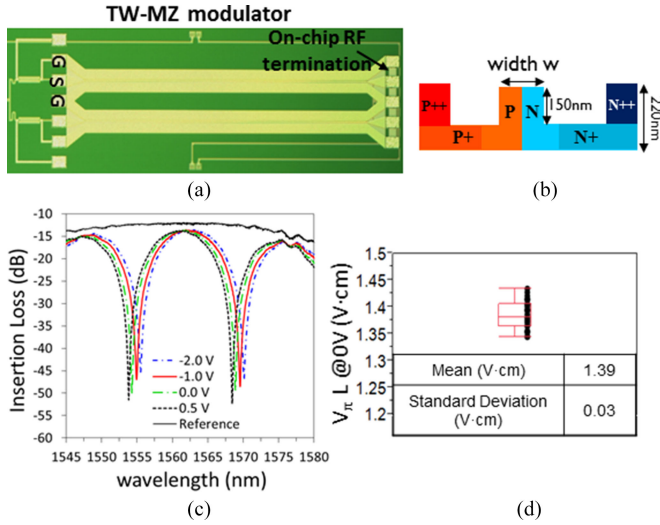


Fig. 2. (a) Top-view microscope image of the TW-MZ modulator with on-chip termination. (b) Schematic cross-section of the MZ modulator waveguide with p-n diode. (c) DC electro-optical response of a lumped MZ test structure, normalized to the power at the input of the grating coupler. (d) Wafer-level distribution of $V_{\pi}L$ of a lumped MZ test structure measured across 14 dies on a 200 mm wafer.

absorption modulators and photodetectors. Standard CMOS Ni-silicide and tungsten (W) contacts are used for contacting the highly doped silicon regions. Thermal control of wavelength-sensitive devices such as silicon ring modulators is enabled by a tungsten heater module. This is processed similarly to W-contacts, before further back-end-of-line processing [10]. Standard Cu damascene metallization is used for the metal interconnects, while an Al-based bond pad and SiN passivation module is used to improve reliability and to enable wire-bonding on the Cu lines. More details on the integration can be found in [8], [9]. For all the devices presented in this work, light is coupled in the Si waveguides using simple fiber grating couplers (FGCs) formed in the c-Si layer, with an average insertion loss of 4.5 dB per FGC at 1550 nm wavelength.

III. TRAVELLING-WAVE MACH-ZEHNDER MODULATOR

Fig. 2(a) shows a top-view image of the travelling-wave Mach-Zehnder (TW-MZ) modulator fabricated in imec's 200 mm silicon photonics platform. The depletion-type phase shifter is formed by a p-n doped rib waveguide of 450 nm width and 220 nm height for C-band operation, as shown in Fig. 2(b). The p- and n- doped areas of the waveguide have a nominal concentration in the range of $0.5\text{--}5 \times 10^{18}/\text{cm}^3$, depending on the modulator type. A 70 nm Si slab, p^+ - or n^+ - doped at $3 \times 10^{19}/\text{cm}^3$, is used to electrically connect the waveguide embedded p-n junction to the highly p^{++} or n^{++} doped ($3 \times 10^{20}/\text{cm}^3$) contact regions. These doping conditions were chosen to improve the device bandwidth by reducing the series resistance, while balancing the device capacitance with sufficient electro-optic modulation efficiency. The typical figure of merit to characterize modulation efficiency of a phase-shifter modulator is the $V_{\pi}L$ -product, where L is the device length and V_{π} is the voltage swing required to achieve a π -phase shift. The DC electro-optical response of a phase shifter with optimized

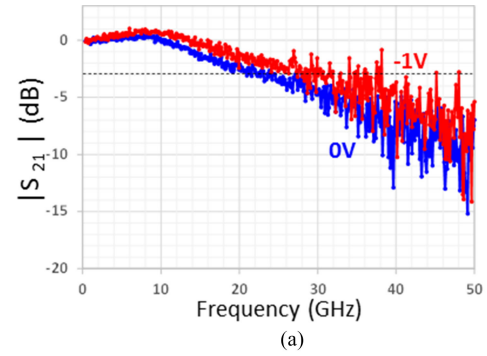


Fig. 3. (a) S_{21} electro-optical response of the TW-MZ modulator at 0 V and -1 V bias. 56 Gb/s eye diagram with (b) ER = 2.3 dB and SNR = 3.3 at quadrature point and (c) ER = 4.1 dB and SNR = 4.8 operating 4 dB away from quadrature point, obtained using the TW-MZ modulator with on-chip termination, driven by 2.5 V_{pp}.

doping conditions measured on a lumped Mach-Zehnder test structure of 1.5 mm length, is $V_{\pi}L = 1.39$ V·cm, as shown in Fig. 2(c), while the optical propagation loss is 14.7 dB/cm, resulting in a 20.4 V·dB efficiency-loss product. The wafer-level distribution of the $V_{\pi}L$ figure of merit across a 200 mm wafer has a standard deviation of 0.03 V·cm (Fig. 2(d)). The capacitance of the phase shifter with the above doping conditions is 0.378 fF/ μm at 0 V and 0.275 fF/ μm at -2 V, as extracted by capacitance-voltage measurements at 100 kHz.

The TW-MZ modulator design has coplanar waveguide electrodes (CPW) above the 1.5 mm long phase shifter, which are used to drive the modulator. The width of the signal metal is 5.2 μm , while the distance between the signal line and each ground line is 3 μm . To improve the device bandwidth, an on-chip RF termination is implemented at the n^{++} -doped layer [11]. This consists of an area of 40 μm long and 40 μm wide n^{++} doped Si, targeting 50 Ohm resistance. Two 50-Ohm resistors, each connected between the signal and the ground on the Ground-Signal-Ground pad configuration are implemented, resulting in 25 Ohm termination on the TW-MZ modulator. The efficiency of the TW-MZ modulator is estimated from the lumped Mach-Zehnder phase-shifter response after taking into account the voltage drop over the on-chip termination, resulting in $V_{\pi} = 10.8$ V. The optical insertion loss (IL) of the TW-MZ modulator is ~ 2.2 dB at the maximum of the transmission spectrum, when normalized against a reference waveguide.

The electro-optical small-signal frequency response of the TW-MZ modulator was measured in the C-band using a 50 GHz Keysight lightwave component analyzer and RF power of -8 dBm. A typical S_{21} -parameter measurement is shown in Fig. 3(a). The 3-dB bandwidth is measured to be 22 GHz and 27 GHz at 0 V and -1 V bias, respectively. The large signal modulation performance was measured using single-ended probe and an Anritsu MP1821 50G/56 Gb/s MUX pulse pattern

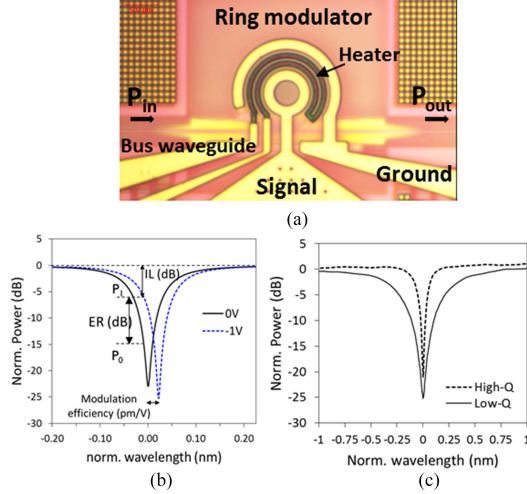


Fig. 4. (a) Top-view microscope image of the silicon ring modulator. (b) Example of ring modulator spectra indicating the figures of merit. (c) Comparison of the normalized zero-bias spectra of the High-Q and Low-Q ring modulators.

generator to drive the TW-MZ modulator with a $2^{31}-1$ Pseudo-Random-Bit-Sequence (PRBS) of NRZ drive voltage having a nominal 2.5 V peak-to-peak (V_{pp}) swing and -0.75 V DC bias. After optical amplification and filtering, eye diagrams were monitored using a Keysight optical module with 40 GHz bandwidth. Open eye diagrams were obtained at 56 Gb/s with 2.2 dB and 4.1 dB dynamic extinction ratio (ER) at and 4 dB away from quadrature point respectively (Fig. 3(b) and (c)). Larger dynamic ER is expected when using a differential drive scheme. Under the single-ended drive conditions, the TW-MZ modulator has an estimated static power consumption of 63.9 mW for voltage swing from 0.5 V to -2 V. The dynamic energy consumption is estimated as $E = C_d V_{pp}^2 / 4$, where C_d is the phase-shifter capacitance and V_{pp} is the peak-to-peak voltage swing [12]. Using this equation and measured capacitance value of $C_d \sim 0.32$ fF/ μ m for -0.75 V bias, the TW-MZ modulator dynamic energy consumption is estimated to be ~ 750 fJ/bit at 56 Gb/s.

IV. SILICON RING MODULATOR

Silicon ring modulators operating in depletion mode can provide low-voltage operation at high bit-rates, using small foot-print, at the expense of narrow optical bandwidth and the need for thermal control for wavelength stability. A typical top-down microscope image of a silicon ring modulator is shown in Fig. 4(a). The ring waveguide incorporates a p-n junction formed by ion implantation of the silicon, similar to the one shown in Fig. 2(b). In reverse bias, the carriers are depleted from the p-n junction in the ring waveguide, resulting in refractive index and absorption changes in silicon [13], shifting the ring resonance wavelength to longer wavelengths. Operating in depletion mode results in weaker modulation efficiency as compared to carrier-injection based p-i-n ring modulators, however with the advantage of **lower device capacitance enabling high speed operation with simple drive circuits [7]**. The temperature sensitivity of silicon imposes the need for integrated heaters to control the operating wavelength of the ring modulators upon temperature

fluctuations [14]. In imec's silicon photonics platform, tungsten heaters are integrated above the ring modulator (Fig. 4(a)), after contacts and before the first metal layer in the integration flow, as shown in the schematic of Fig. 1.

A. Figures of Merit

Fig. 4(b) shows typical ring modulator spectra at 0 V and -1 V. We define the modulation efficiency (ME) as the ring resonance wavelength shift achieved per voltage of applied bias, in pm/V. The system level characteristics that we use to describe the performance of a ring modulator are the extinction ratio ER (dB) $= 10\log(P_1/P_0)$, and the transmitter penalty TP (dB) $= 10\log(2P_{IN}/(P_1 - P_0))$, where P_1 and P_0 are the power transmitted during a 1-bit, and during a 0-bit, respectively, and P_{IN} is the input optical power [15].

The frequency response of the ring modulators is governed by the p-n junction RC response and the photon dynamics in the ring waveguide. Detailed analysis of the photon dynamics and the wavelength dependence of the ring modulator frequency response has been presented recently by different groups [16]–[18]. Here we use the simplified model for the ring modulator 3 dB bandwidth ($f_{3\text{ dB}}$) where the cavity photon lifetime and the RC time delay act as low-pass filters, described by the equation $1/f_{3\text{ dB}}^2 = 1/f_Q^2 + 1/f_{RC}^2$, to identify the dominant factor limiting the modulator frequency response. The first component in this equation is the frequency limitation due to cavity photon lifetime (τ) given by $f_Q = 1/2\pi\tau$ where $\tau = Q\lambda/2\pi c$ depends on the Q-factor of the ring, λ is the operating wavelength and c is the speed of light in vacuum. The second component is the junction RC delay described by $f_{RC} = 1/(2\pi RC)$. In order to achieve high modulation bandwidth, it is therefore necessary to reduce the ring modulator Q-factor, as well as the resistance and the capacitance of the p-n junction. **Increasing the doping in the ring modulator will reduce the Q-factor and resistance, at the expense of increased capacitance.** However, reducing the Q factor typically also reduces the extinction ratio and increases the insertion loss of the ring modulator. Hence, a trade off exists between modulation bandwidth and modulator optical loss.

B. Device Description and DC results

The impact of Q-factor is investigated by comparing two cases of doping concentrations in the p-n junction resulting in a low-doped (high Q-factor) and a highly-doped (low Q-factor) ring modulator. The ring modulators were fabricated using imec's 300 mm silicon photonics platform. **The 500 nm wide ring waveguide was formed by etching the silicon by 150 nm**, which enabled **ring resonators of 5 μ m radius** with a free-spectral range of **19.3 nm**, suitable for WDM applications. Such a small ring size translates in lower device capacitance, which can reduce the RC bandwidth limitation. To reduce the etched-silicon trench and contact resistance, doping concentrations of $4.5 \times 10^{19} \text{ cm}^{-3}$ and $3 \times 10^{20} \text{ cm}^{-3}$ were used respectively. Ring modulators with nominal doping concentrations of **$2 \times 10^{18} \text{ cm}^{-3}$** (the “High-Q” ring modulator) and **$5 \times 10^{18} \text{ cm}^{-3}$** (the “Low-Q” ring modulator) in the p-n junction are compared here in terms of performance. The bus-ring spacing was adjusted in each case for critical coupling,

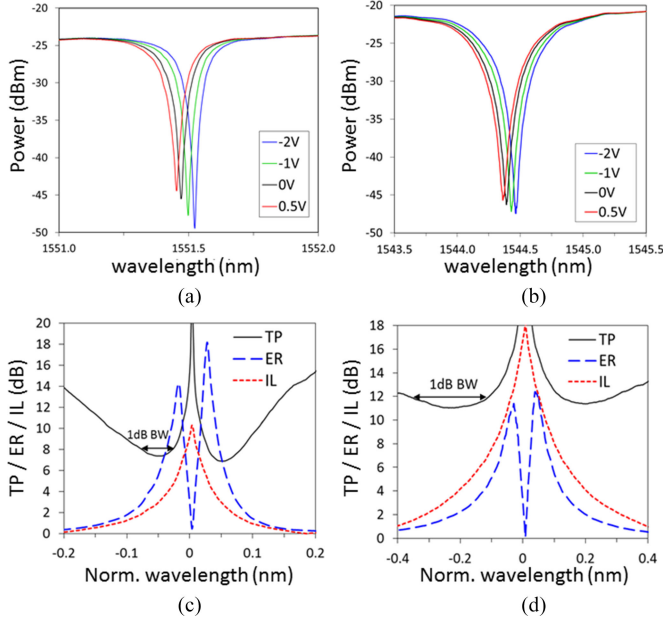


Fig. 5. Transmission spectra of (a) the High-Q and (b) the Low-Q ring modulator at different voltages. Transmitter penalty, extinction ratio and insertion loss spectra for (c) the High-Q and (d) the Low-Q ring modulator, calculated assuming a voltage change from 0.5 V to -1 V. The 1 dB bandwidth from the minimum transmitter penalty is indicated by the arrows in (c) and (d).

to 230 nm and 150 nm spacing for the High-Q and Low-Q ring modulator respectively.

Fig. 4(c) shows a comparison of the zero-bias ring spectra centered around their resonance wavelength, indicating the difference in Q-factor and a transmission extinction beyond 20 dB at resonance. The Q-factor was 9900 for the High-Q and 2200 for the Low-Q ring modulator, which correspond to cavity photon lifetime frequency limitations of $f_Q \sim 19.5$ GHz and ~ 88 GHz, respectively. An example of the ring modulator spectra at varying bias measured at the central die are shown in Fig. 5(a) and (b). For a voltage shift from 0.5 V to -1 V (corresponding to 1.5 V peak-to-peak), which can be obtained from simple, low-power CMOS circuits [7], the resonance shift for these dies was 45.2 pm and 67.6 pm for the High-Q and Low-Q ring modulator, corresponding to modulation efficiencies of 30.1 pm/V and 45.1 pm/V respectively. Increasing the doping in the p-n junction increases the modulation efficiency, since there are more carriers to be depleted now from the waveguide owing to the larger depletion capacitance, which to some extent counteracts the lower extinction ratio achieved for lower Q-factor. A comparison of the extinction ratio and insertion loss versus wavelength offset from the zero-bias resonance wavelength is shown in Fig 5(c) and (d). The transmitter penalty of the two ring modulators, calculated from the DC data assuming a voltage swing from 0.5 V to -1 V, is also plotted in Fig. 5(c) and (d). The minimum transmitter penalty does not coincide in wavelength with maximum extinction ratio, due to the increased loss when moving closer to the ring resonance. Both the value and the wavelength location of minimum transmitter penalty depend on the Q-factor of the ring. For the High-Q and Low-Q ring modulators of this work minimum transmitter penalties of

TABLE I
RING MODULATOR STATIC PERFORMANCE FOR 0.5 V TO -1 V VOLTAGE SWING

Device	ME (pm/V)	Min. TP (dB)	1 dB BW (pm)	ER at min TP (dB)	IL at min TP (dB)
High-Q	30.1	6.9	50	6.6	2.8
Low-Q	45.1	11	263	1.8	3.3

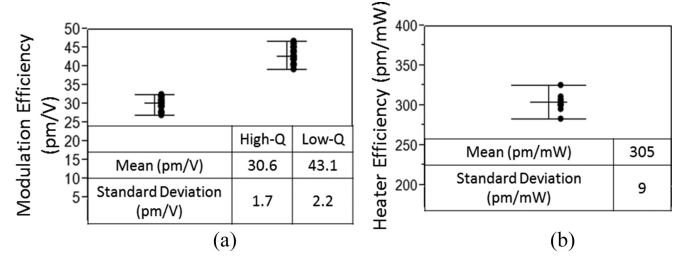


Fig. 6. (a) Modulation efficiency and (b) W-heater efficiency from a Low-Q ring modulator measured across 25 dies on a 300 mm wafer.

6.9 dB and 11 dB were extracted from the measurements. The increased loss due to higher carrier concentration in the Low-Q ring modulator results in 4 dB increase in the transmitter penalty. However, when comparing the 1 dB bandwidth from the minimum transmitter penalty, this increases by more than 5 times, from 50 pm for the High-Q to 260 pm for the Low-Q ring modulator, which can relax the requirements for thermal control of the ring resonance wavelength, potentially reducing the overhead cost. The static performance characteristics of the two modulators are summarized in Table I for voltage swing from 0.5 V to -1 V. Wafer-scale measurements of the modulation and the W-heater efficiency, as measured from 25 dies across a 300 mm wafer are shown in Fig. 6. The mean modulation efficiency across the wafer was 30.6 pm/V with standard deviation (1σ) of 1.7 pm/V and 43 pm/V with 1σ of 2.2 pm/V for the High-Q and Low-Q ring modulator respectively. The mean heater efficiency was 305 pm/mW with 1σ of 9 pm/mW across the wafer. This value of heater efficiency corresponds to heater power consumption of 63.3 mW for shifting the resonance of a 5 μ m ring across one free-spectral range. By implementing improved thermal isolation, i.e. by locally removing the Si substrate below the ring modulator, the heater efficiency can be improved [19], [20].

C. High Speed Characterization

The small-signal response of the High-Q and Low-Q ring modulators was measured as described in Section III. The results from the electrical S_{11} response at 0 V are shown in Fig. 7(a) for the Low-Q ring modulator. The S_{11} response was fitted by the simple electrical model also shown in Fig. 7(a). In this model, C_1 and R_1 are the ring modulator capacitance and series resistance, and C_0 , C_2 and R_2 describe the parasitic pad capacitance and resistance. Table II shows the values of the circuit components that resulted in optimum fitting. A significant reduction in the ring modulator resistance is achieved by increasing the doping concentration, accompanied by ~ 8 fF increase in

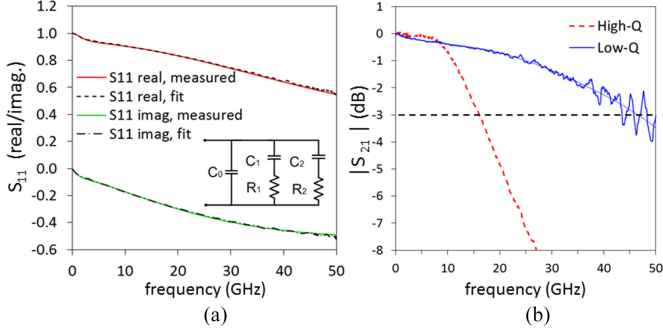


Fig. 7. (a) Electrical S_{11} at 0 V of Low-Q ring modulator measured and fitted using the inset model. (b) Electro-optical S_{21} response at 0 V.

TABLE II

ELECTRICAL PARAMETERS OF THE RING MODULATOR EQUIVALENT CIRCUIT OBTAINED FROM FITTING TO S_{11} AND MODULATION BANDWIDTH FROM S_{21} MEASUREMENTS

Device	Bias	C_1 (fF)	R_1 (Ohm)	C_2 (fF)	R_2 (Ohm)	C_0 (fF)	f_{3dB} (GHz)
High-Q	0 V	15	177	52	1160	6.5	16
Low-Q	0 V	22.7	65	55	1380	5	47

capacitance. The dynamic energy consumption for 1.5 V voltage swing calculated from these values is 8.4 fJ/bit and 12.8 fJ/bit for the High-Q and Low-Q ring modulator respectively.

The measured electro-optical S_{21} response at 0 V bias is shown in Fig. 7(b). Given the wavelength dependence of the ring modulator frequency response, the value reported here is at the wavelength of minimum transmitter penalty. Minimum transmitter penalty corresponds to maximum optical modulation amplitude (OMA) and hence maximum S_{21} magnitude measured by the lightwave component analyzer. The measured 3 dB electro-optical bandwidth of the High-Q and Low-Q ring modulators was ~ 16 GHz and 47 GHz respectively. From the values of Table II the RC frequency limit f_{RC} can be estimated as 43 GHz and 51 GHz for the High-Q and Low-Q ring modulator respectively. This indicates that the frequency response of the High-Q ring modulator is limited by the cavity photon lifetime, while the Low-Q modulator response is limited by RC.

The modulator performance of the Low-Q ring modulator was further tested by means of large-signal high-frequency modulation using a PRBS of $2^{31}-1$ pattern length. The ring modulator was driven using a 67 GHz RF probe with a 50 Ω termination, to limit back reflections. Fig. 8(a)–(d) show eye diagrams obtained at 50 Gb/s with 1.5 V_{pp} voltage swing and –0.25 V bias at wavelengths from 1544.6 nm to 1544.9 nm. Open eye diagrams are obtained across this wavelength range with signal-to-noise ratio of ~ 6 . This demonstrates that the Low-Q ring modulator can relax the strict wavelength control typically required to preserve signal integrity upon temperature fluctuations, when using ring modulators. Open eye diagrams are also shown with 1 V_{pp} swing at 50 Gb/s and at 56 Gb/s in Fig. 8(e) and (f), which is the maximum bit-rate that can be reached by the measurement equipment available. The dynamic energy consumption of the Low-Q modulator for 1 V_{pp} voltage swing was estimated at 5.7 fJ/bit, corresponding to 0.32 mW power consumption

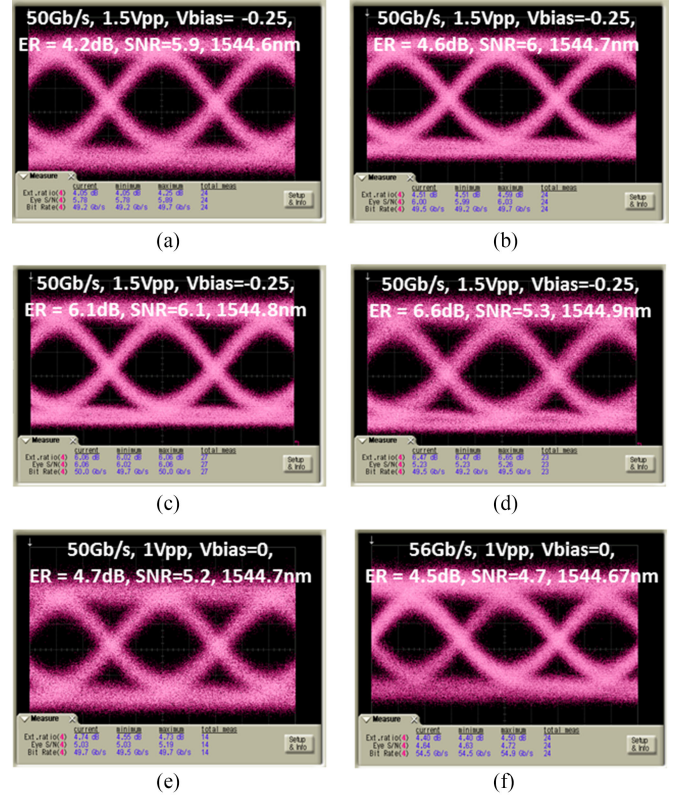


Fig. 8. Eye diagrams obtained with the Low-Q silicon ring modulator at different operating conditions, using an NRZ PRBS $2^{31}-1$ signal: (a)–(d) 50 Gb/s with 1.5 V_{pp} swing, V_{bias} = –0.25 V, varying wavelength, (e) 50 Gb/s with 1 V_{pp} swing, V_{bias} = 0 V, (f) 56 Gb/s with 1 V_{pp} swing, V_{bias} = 0 V.

at 56 Gb/s. With a free spectral range of 19.3 nm, the Low-Q modulator could potentially be implemented in an 8×56 Gb/s cascaded WDM transmitter.

V. GE BASED ELECTRO-ABSORPTION MODULATOR

Electro-absorption modulators (EAMs) using Ge or GeSi exploit the Franz-Keldysh (FK) effect to modulate a laser beam [15]. The FK effect is driven by the electric field intensity and modulates the absorption coefficient at wavelengths close to the direct band gap edge of bulk Ge or GeSi. As a result, for an electric field difference of 5×10^4 V/cm between the ON and OFF states, realized with the implementation of a p-i-n diode operated in reverse bias, the absorption coefficient is modified by a factor of 3 [21], [22].

In imec's silicon photonics platform, light is coupled from the 220 nm-thick silicon waveguide to the Ge waveguide via tapers in the poly-silicon layer. The Ge waveguide comprises a p-i-n diode operating in reverse bias, contacted through the doped silicon regions. Ge and GeSi waveguide EAMs of 600 nm width and 40 μ m length are discussed in this section. The only difference between the two devices is the thickness of the active layer. The Ge EAM has a Ge thickness of 350 nm while the GeSi EAM has a GeSi thickness of 300 nm [21], [22]. Bulk Ge grown on Si using imec's 200 mm Si photonics platform has a band-gap of 1580–1590 nm allowing modulation around 1615 nm wavelength. By incorporation of $\sim 0.8\%$ Si in the

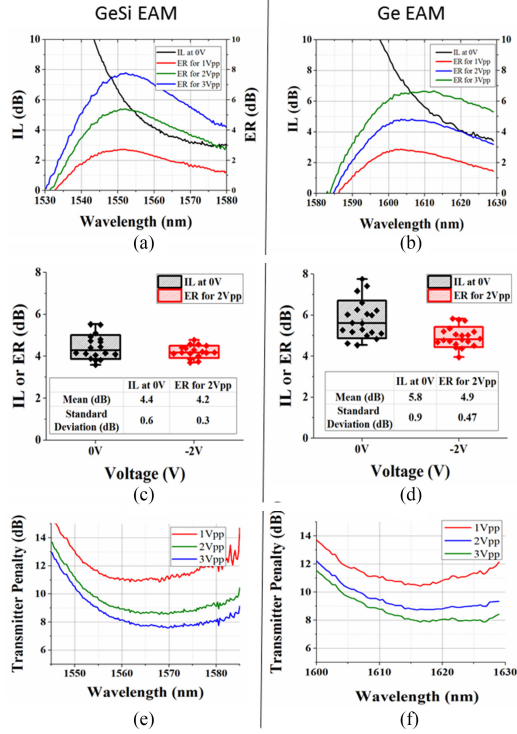


Fig. 9. (a), (b). Extracted insertion loss (IL) and extinction ratio (ER) spectra assuming 1 Vpp, 2 Vpp and 3 Vpp for a 0.6 μm wide and 40 μm long Ge and GeSi EAM respectively from [21], [22]. (c) and (d) IL and ER at 1560 nm for the GeSi EAM and at 1615 nm for the Ge EAM across 20 dies on a 200 mm SOI wafer. The box edge represents the standard deviation of the measured data. (e) and (f) Transmitter penalty for 1 Vpp, 2 Vpp and 3 Vpp extracted from (a) and (b).

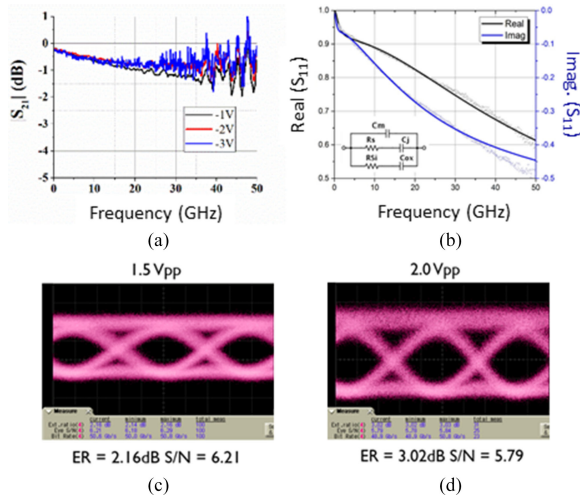


Fig. 10. (a) RF S_{21} measurements of GeSi EAM with 3 dB electro-optical response beyond 50 GHz at -1 V, -2 V and -3 V bias from [21]. (b) RF S_{11} measurement of GeSi EAM at -1 V (symbols) and fitting (lines) from [21]. Eye diagrams measured with the GeSi EAM at 1560 nm with (c) 1.5 Vpp and (d) 2.0 Vpp voltage swing at the data rate of 50 Gb/s from [21].

bulk Ge, the direct bandgap is shifted to 1535 nm enabling C-band modulation around 1565 nm at room temperature. This is verified by the static modulator measurements shown in Fig. 9. Fig. 9(a) and (b) shows the insertion loss and extinction ratio spectra for the Ge and GeSi EAMs assuming 1 Vpp, 2 Vpp and

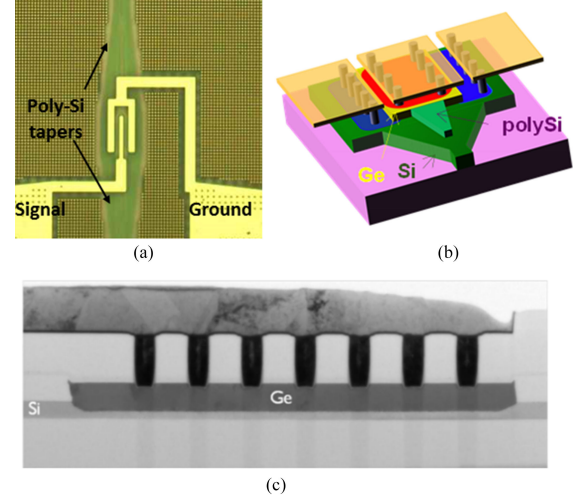


Fig. 11. (a) Top-view microscope image and (b) schematic of a Ge photodetector. (c) TEM cross-section along a 15 μm long Ge photodetector.

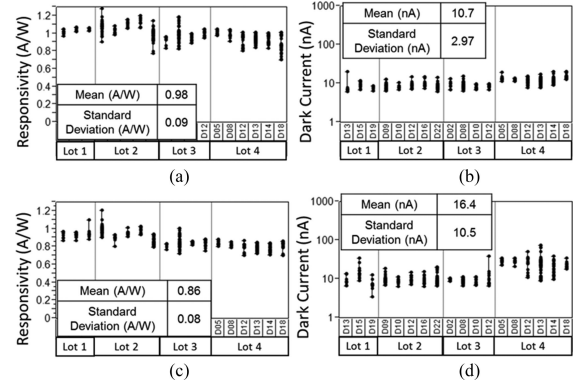


Fig. 12. Responsivity at 1550 nm and dark current of Ge PD-1 (a, b) and of Ge PD-2 (c, d) respectively, measured across four fabrication runs and different wafers.

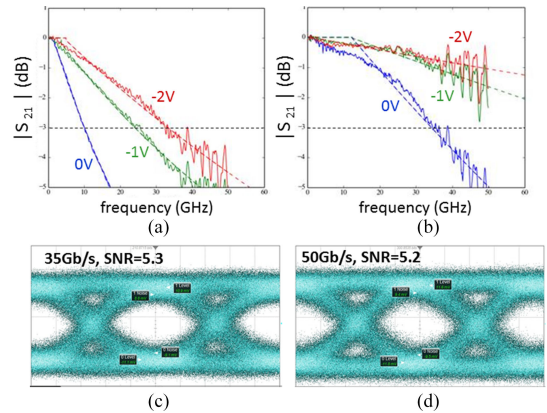


Fig. 13. RF S_{21} response from (a) Ge PD-1 and (b) Ge PD-2. (c) 35 Gb/s eye diagram measured with the Ge PD-1 at -2 V bias. (d) 50 Gb/s eye diagram measured with the Ge PD-2 at -2 V bias.

3 Vpp voltage swing, from 0 to -1 V, from 0 to -2 V, and from 0 to -3 V respectively. Wafer-level measurements of the IL and ER, measured on 20 dies across a 200 mm wafer are shown in Fig. 9(c) and (d). IL of 5.8 ± 0.9 dB and ER at -2 V of 4.9 ± 0.5 dB are measured for the Ge EAM at 1615 nm. The GeSi EAM has similar performance, with IL of 4.4 ± 0.6 dB and ER

TABLE III
SUMMARY OF HIGH-SPEED MODULATOR PERFORMANCE DEMONSTRATED IN THIS PAPER

Modulator type	Footprint $\mu\text{m} \times \mu\text{m}$	Wavelength nm	Optical Range nm	Dynamic ER dB	Dynamic IL dB	Voltage Swing V	Power consumption		3 dB bandwidth (at bias) GHz (V)	Measured Bit rate Gb/s	SNR at bit rate
							Static mW	Dynamic fJ/bit			
TW-MZ Modulator	$\sim 2000 \times 500$	1300/1500	> 80	2.3	~ 5.2	2.5	63.9	750	22 (at 0 V)	56	3.3
Si ring	$\sim 10 \times 10$	1300/1500	~ 0.3	6.1	~ 8.4	1.5	63.3 (for heater)	12.8	47 (at 0 V)	50	4.8
modulator				4.5	~ 10.1	1		5.7		56	6.1
GeSi FK EAM	$\sim 40 \times 10$	1560	~ 30	2.2	~ 4.4	1.5	~ 1.17	7.8	> 50	50	4.7
				3	~ 4.4	2	1.7	13.8	(at -1 V)		6.2
											5.8

at -2 V of 4.2 ± 0.3 dB, measured at 1560 nm. Fig. 9(e) and (f) shows also the extracted transmitter penalty spectra for the Ge and GeSi EAM at 1 V_{pp}, 2 V_{pp} and 3 V_{pp}. Minimum transmitter penalties of 8.5 dB at around 1565–1570 nm for the GeSi EAM and 9.1 dB at around 1615–1620 nm for the Ge EAM were extracted for 2 V_{pp} with 1 dB optical bandwidth of up to 30 nm. Ge-based EAMs therefore offer the advantage of larger optical bandwidth compared to silicon ring modulators.

Electrical S_{11} and electro-optic S_{21} measurements of the Ge-based modulators were performed using a 50 GHz lightwave component analyzer. 3-dB bandwidth greater than 50 GHz was measured for the GeSi EAM for reverse bias voltage above 1 V as shown in Fig. 10(a). Similar performance was observed for the Ge EAM [21]. As FK effects are sub-picosecond effects, the speed of the modulator is limited by the RC time constant of the device [21], [23]. By fitting the RF S_{11} measurement with the equivalent circuit model shown in Fig. 10(b), the electrical parameters of the devices were extracted. The junction capacitance is estimated to be 13.8 fF and 12.8 fF and the series resistance 220 Ω and 280 Ω at -1 V for the GeSi and Ge EAM respectively, suggesting an RC limited bandwidth beyond 50 GHz. The relatively small cross section and length of the Ge-based modulators result in low junction capacitance, suitable for high speed operation, without compromising the modulation efficiency. This is verified by large signal modulation measurements as shown in Fig 10(c) and (d), where a PRBS with a pattern length of $2^{31}-1$ at 50 Gb/s was applied on the device. Open eye diagrams with dynamic ER of 2.2 dB and 3 dB for 1.5 V_{pp} and 2 V_{pp} respectively were obtained for the GeSi EAM at 1560 nm with signal-to-noise ratio greater than 5 [22].

The static power consumption of an electro-absorption modulator is related to the photo-current and dark current of the device as $\frac{1}{2}(I_{\text{on}}V_{\text{on}} + I_{\text{off}}V_{\text{off}})$ [12]. The dynamic power consumption, defined as the amount of power required to switch the ON and OFF state of the modulator, is estimated by calculating the average dynamic energy consumption per bit as $E = C_d V_{\text{pp}}^2 / 4$ [12]. The eye diagram measurements were performed with an input optical power of 3 dBm on the GeSi EAM, resulting in photocurrent of 1.7 mA at -2 V. This corresponds to 1.7 mW average static power consumption. With $C_d = 13.8$ fF at bias voltage of -1 V for 2 V_{pp}, the dynamic energy consumption per bit is estimated at 13.8 fJ/bit, which translates

to 0.69 mW at 50 Gb/s data transmission rate. As a result, the total power consumption (dynamic and static) is 2.39 mW for 2 V_{pp} operation at 50 Gb/s.

VI. GE PHOTODETECTORS

The Ge waveguide photodetectors (PDs) are integrated in the silicon photonics platform in a similar way as the Ge EAMs, i.e. using tapers in the poly-silicon layer to couple light from the silicon to the Ge waveguide. Fig. 11 shows a top-view microscope image, a schematic design of the device and a TEM cross-section along the 15 μm device length of the Ge PD. The Ge PDs comprise a vertical p-i-n diode, with the p-doped (10^{20} cm^{-3}) area later formed in the Ge by shallow ion implantation. The n-doped area (10^{19} cm^{-3}) of the diode is formed in the underlying silicon layer. Depending on the contact scheme, the device performance can be engineered towards higher responsivity or higher bandwidth [8], [24], [25]. Here we compare two cases, referred to as Ge PD-1 and Ge PD-2. The two designs have Ge width of 2 μm , lengths of 13.7 μm and 15.2 μm , and contact pitch of 0.9 μm and 0.6 μm respectively. When the contact pitch is larger there are less contacts on the Ge, resulting in more interaction of the light with the Ge and less absorption by the metals. This effect is stronger than the small difference in length. Fig. 12 compares the responsivity and dark current of the two designs as measured across four fabrication runs and across a number of wafers. Ge PD-1 has a mean responsivity value and standard deviation (1σ) of 0.98 ± 0.09 A/W at 1550 nm wavelength and -1 V bias, while the dark current is 10.7 ± 3 nA. For Ge PD-2 the mean responsivity drops to 0.86 ± 0.08 A/W and the dark current increases to 16.4 ± 10.5 nA.

Fig. 13(a) and (b) shows the S_{21} measurements of the two Ge PDs at 0 V, -1 V and -2 V, measured with a 50 GHz lightwave component analyzer. Ge PD-1 has a 3 dB bandwidth of 10 GHz, 24 GHz, and 33 GHz at 0 V, -1 V, and -2 V respectively. Ge PD-2 has a 3 dB bandwidth of 35 GHz at 0 V, while at larger reverse bias it exceeds 50 GHz. Large-signal characterization was performed using a 44 GHz commercial modulator generating an NRZ signal with $2^{31}-1$ PRBS data pattern length at bit-rates varying from 25 Gb/s to 50 Gb/s. The electrical data output from the Ge PDs were measured using an oscilloscope with a 60 GHz remote sampling head. Open eye diagrams at

TABLE IV
SUMMARY OF PHOTODETECTOR PERFORMANCE IN THIS PAPER

PD type	Responsivity	Dark Current	3 dB bandwidth (at -1 V)	Bit rate	SNR
	A/W	nA	GHz	Gb/s	
Ge PD-1	0.98	10.7	24	35	5.3
Ge PD-2	0.86	16.4	> 50	50	5.2

-2 V bias were obtained at 35 Gb/s and 50 Gb/s using Ge PD-1 and Ge PD-2 respectively, as shown in Fig. 13(c) and (d).

VII. CONCLUSIONS

In this paper we reviewed recent progress on the active components of imec's silicon photonics platform. Tables III and IV show a performance comparison of the three modulator types and the two photodetector designs described in this work. By optimizing the design and process flow, high NRZ bit-rates of 50–56 Gb/s can be achieved by each modulator type with different trade-offs between footprint, optical operation range, fabrication complexity, voltage swing and bandwidth. Similarly, a trade-off exists between Ge PD responsivity/dark current and speed. By improving the device design, adjusting the implant conditions and reducing the device size, bit rates ≥ 50 Gb/s were achieved by a variety of components, at the expense of lower ER/higher IL for the modulators or lower responsivity/higher dark current for the Ge PDs. These components can be tailored to fabricate high-speed SDM or WDM transceivers operating at CMOS compatible voltages.

ACKNOWLEDGMENT

The authors acknowledge imec's 200 mm and 300 mm pilot-line for contribution to device fabrication, as well as imec's PDK team. This work was supported by imec's Core Partner Program.

REFERENCES

- [1] A. V. Krishnamoorthy, H. Schwetman, X. Zheng, and R. Ho, "Energy-efficient photonics in future high-connectivity computing systems," *IEEE J. Lightw. Technol.*, vol. 33, no. 4, pp. 889–900, Feb. 15, 2015.
- [2] S. Rumley *et al.*, "Silicon photonics for exascale systems," *IEEE J. Lightw. Technol.*, vol. 33, no. 3, pp. 547–562, Feb. 1, 2015.
- [3] B. R. Koch *et al.*, "A 4×12.5 Gbps CWDM si photonics link using integrated hybrid silicon lasers," in *Conf. Lasers Electro-Optics, OSA Tech. Dig.*, 2011, Paper CThP5.
- [4] H. Liu, "Integrated silicon photonics links for high bandwidth data transportation," in *Optical Fiber Commun. Conf. Exhib. OSA Tech. Dig.*, 2014, Paper Th1D.1.
- [5] T. Takemoto *et al.*, "A 50 Gb/s NRZ-modulated optical transmitter based on a DFB-LD and a $0.18 \mu\text{m}$ SiGe BiCMOS LD driver," in *Opt. Fiber Commun. Conf.*, Los Angeles, CA, USA, 2015, Paper Tu3G.2.
- [6] B. G. Lee *et al.*, "A WDM-compatible 4×32 Gb/s CMOS-driven electro-absorption modulator array," in *Optical Fiber Commun. Conf.*, 2015, Paper Tu3G.3.
- [7] M. Rakowski *et al.*, "22.5 A 4×20 Gb/s WDM ring-based hybrid CMOS silicon photonics transceiver," in *Proc. IEEE Int. Conf. Solid-State Circuits*, San Francisco, CA, USA, Feb. 22–26, 2015, pp. 1–3.
- [8] P. Verheyen *et al.*, "Highly uniform 25 Gb/s si photonics platform for high-density, low-power WDM optical interconnects," in *Proc. Integrated Photon. Res., Silicon Nanophoton.*, Jul. 2014, Paper IW3A.4, pp. 13–17.
- [9] P. Absil *et al.*, "Imec iSiPP25G silicon photonics: A robust CMOS-based photonics technology platform," in *Proc. SPIE*, vol. 9367, Feb 2015, Art. no. 93670V (6 pages), doi:10.1117/12.2076262.
- [10] A. Masood *et al.*, "Fabrication and characterization of CMOS-compatible integrated tungsten heaters for thermo-optic tuning in silicon photonics devices," *Opt. Mater. Express*, vol. 4, no. 7, pp. 1383–1388, Jul. 2014.
- [11] H. Yu and W. Bogaerts, "An equivalent circuit model of the traveling wave electrode for carrier-depletion-based silicon optical modulators," *J. Lightw. Technol.*, vol. 30, no. 11, pp. 1602–1609, Jun. 2012.
- [12] D. A. B. Miller, "Energy consumption in optical modulators for interconnects," *Opt. Express*, vol. 20, pp. A293–A308, 2012.
- [13] R. A. Soref and B. R. Bennett, "Electrooptical effects in silicon," *IEEE J. Quantum Electron.*, vol. QE-23, no. 1, pp. 123–12, Jan. 1987.
- [14] S. Agrawal *et al.*, in *Optical Fiber Commun. Conf. OSA Tech. Dig.*, 2016, Paper Th1F.5.
- [15] D. Feng *et al.*, "High-speed GeSi electroabsorption modulator on the SOI waveguide platform," *IEEE J. Sel. Top. Quantum Electron.*, vol. 19, no. 6, pp. 64–73, Nov./Dec. 2013.
- [16] W. Sacher and J. K. S. Poon, "Dynamics of microring resonator modulators," *Opt. Express*, vol. 16, no. 20, pp. 15741–15753, Sep. 2008.
- [17] H. Yu *et al.*, "Trade-off between optical modulation amplitude and modulation bandwidth of silicon micro-ring modulators," *Opt. Express*, vol. 22, no. 12, pp. 15178–15189, Jun. 2014.
- [18] J. Muller *et al.*, "Optical peaking enhancement in high-speed ring modulators," *Sci. Rep.*, vol. 4, Aug. 2014, Art. no. 6310, doi:10.1038/srep06310.
- [19] P. Dong *et al.*, "Thermally tunable silicon racetrack resonators with ultralow tuning power," *Opt. Express*, vol. 18, no. 19, pp. 20298–20304, Sep. 2010.
- [20] X. Zheng *et al.*, "A high-speed, tunable silicon photonic ring modulator integrated with ultra-efficient active wavelength control," *Opt. Express*, vol. 22, no. 10, pp. 12628–12633, May 2014.
- [21] S. A. Srinivasan *et al.*, "56 Gb/s germanium waveguide electro-absorption modulator," *IEEE J. Lightw. Technol.*, vol. 34, no. 2, pp. 419–424, Jan. 15, 2016.
- [22] A. Srinivasan *et al.*, "50 Gb/s C-band GeSi waveguide electro-absorption modulator," in *Optical Fiber Commun. Conf., OSA Tech. Dig.*, 2016, Anaheim, CA, USA, Paper Tu3D.7.
- [23] D. A. B. Miller, D. S. Chemla, and S. Schmitt-Rink, "Relation between electroabsorption in bulk semiconductors and in quantum wells: The quantum-confined Franz-Keldysh effect," *Phys. Rev. B*, vol. 33, pp. 6976–6982, 1986.
- [24] H. Chen *et al.*, "High responsivity low-voltage 28 Gb/s Ge p-i-n photodetector with silicon contacts," *IEEE J. Lightw. Technol.*, vol. 33, no. 4, pp. 820–824, Feb. 2015.
- [25] H. Chen *et al.*, "Dark current analysis in high-speed germanium p-i-n waveguide photodetectors," *J. Appl. Phys.*, vol. 119, no. 21, 2016, Art. no. 213105.

Authors' biographies not available at the time of publication.